What atomic properties of metal oxide control the reaction threshold of solid elemental fuels?

Journal:	*Physical Chemistry Chemical Physics*
Manuscript ID	CP-ART-03-2018-001671.R1
Article Type:	Paper
Date Submitted by the Author:	30-Aug-2018
Complete List of Authors:	Wang, Xizheng; University of Maryland, Chemical and Biomolecular Engineering; University of Maryland, Chemistry & Biochemistry Zachariah, Michael ; University of Maryland at College Park,

What atomic properties of metal oxide control the reaction threshold of solid elemental fuels?

Xizheng Wang, Michael R. Zachariah[*]

University of Maryland, College Park, Maryland, 20740, United States

Abstract

The redox reaction between fuel (metal, metalloid, etc.) and metal oxide is ubiquitous. On the other hand simple thermodynamic considerations do not seem to yield much insight into what makes for a vigorous oxidizer. In this study, two different systematically doped metal oxide systems: perovskites (9 compounds) and δ-Bi_2O_3 (12 compounds) were synthesized in a manner such that for each system the crystal structure and morphology were maintained. Four fuels (Al, B, Ta, C) with different physical properties, covering almost all fuel types, were included in this study. The initiation temperature and oxygen release temperature was measured by fast heating (> 10^5 K/s) temperature-jump/time-of-flight mass spectrometry coupled with high-speed imaging. These results were then correlated with the average metal-oxygen bond energy in the oxidizer, and overall metal-oxygen electronegativity. In general, within each systematic metal oxide, we found linear relationships between average bond energy and electronegativity of the metal oxides with initiation temperature for all four fuels, despite their very different physical/chemical properties. These results indicate that intrinsic atomic properties of metal oxide control fuel-metal oxide reaction initiation.

Introduction

Metal (Al, Mg, Ti), metalloid (B, Be) or nonmetals (C) are commonly employed as high energy density fuels. Very often the oxidant is an oxygen donor that can be intimately packed together with the fuel. Typically this is a metal oxide, which can under appropriate condition lead to very rapid redox reactions. Nominally with the appropriate fuel-oxidizer pair based on the overall thermodynamics, the reaction once initiated, releases sufficient thermal energy to enable a self-sustainable reaction during this seemingly simple oxygen exchange process. Mass diffusion typically controls the overall reaction rate of these separate entities of solid-state fuel and metal oxide. More recently with the interest in nanoscale materials, the reduced length scale offers the potential to significantly reduce the energy release time (< 1 ms).[1-3] Observationally the initiation temperature is an important easy metric and is the onset temperature of vigorous self-sustaining redox reaction between fuel and metal oxide when the heat release rate overcomes the heat consuption rate. The initiation temperature results from a complex interplay of many variables, most obviously the nature of reactants, but also experimental parameters, e.g. heating rate, experimental configuration and packing. However even for seemingly the same experimental configurations, we and others have found that there can be large differences in initiation temperatures among different fuel-metal oxide formulations.[4-6] Furthermore these differences have not been resolved by correlating to metal-oxygen bond energy, electronegativity, or even heats of reaction. Thus we are left with no clear indicator of what atomic scale properties correlate to the onset of reaction and the rate of propagation.

One reason is that there are a large number of variables that might affect the initiation temperature, including crystal structure, reaction interface area, morphology, particles size, thermal conductivity, heat capacity, etc. In order to deal with this level of complexity, we have recently focused on a doping strategy to manipulate the properties of specific metal oxide system in a subtle, but systematic manner. The basic concept is to keep as many of the other variables constant (e.g. particle size, crystal structure, density).

In prior work, we synthesized two classes of systematically doped metal oxides (doped perovskites and doped δ-Bi_2O_3) in which many of the dependent variables can be held constant.[7-9] Perovskite oxides, generally, ABO_3, have been employed in solid oxide fuel and electrolysis cells (SOFC/SOEC),[10,11] heterogeneous catalysis of hydrocarbon,[12,13] membranes for oxygen separation,[14] and chemical looping combustion as oxygen carriers.[15,16] Perovskites are useful for our study, as it is possible to adjust redox properties by adopting a large number of different A- and B-site cations. δ-Bi_2O_3 has also been explored by us because of its intrinsic high oxygen ion conductivity, partly due to the ~25% oxygen vacancy, which is why it is often used as an electrolyte in SOFC.[17] Pure δ-Bi_2O_3 is not room temperature stable and oxygen ion conductivity is thus reduced.[18] By doping with other oxides, the cubic structure δ-Bi_2O_3 can be stabilized down to room temperature. One interesting feature of Bi_2O_3 is that it is a pure ionic conductor, which implies that we have a direct opportunity to measure the oxygen ion conductivity, not readily available in other systems which are typically mixed ionic and electronic conductors, e.g. perovskite oxides. In a recent work with aluminum as fuel, we found a correlation between oxygen ion conductivity in doped Bi_2O_3 and initiation temperature.[8] In another prior work we showed that the initiation of Al/doped perovskite could be correlated with metal-oxygen bond energy, oxygen vacancy concentration, and electronegativity.[7] However, it is unknown if the correlation is generic or only works for aluminum.

In this study, four different fuels with different physical properties were studied: Al with a low melting point core (Al: 660 °C) and a high melting point passivating shell (Al_2O_3: 2072 °C), B with a high melting point core (B: 2076 °C) and a low melting point passivating oxide (B_2O_3: 450 °C), Ta with a high melting point core (Ta: 3020 °C) and a high melting point passivating oxide (Ta_2O_5: 1872 °C) and C with a high melting point core (C: 3827 °C) but no passivating oxide.[6,19] Doped perovskites and doped δ-Bi_2O_3 were employed as oxygen carriers. The initiation temperatures were measured by temperature-jump/time-of-flight mass spectrometry (T-Jump/TOFMS) and a high-speed camera. These results were then correlated with the average bond energy and overall metal-oxygen electronegativity difference of doped metal oxide. In general, we found linear relationships between average bond energy and electronegativity with initiation temperature for all four fuels despite their wide range of physical/chemical properties.

Experimental

Synthesis of Doped Metal Oxides.

In this study, 9 doped perovskites and 12 doped Bi_2O_3 listed in Table 1 were synthesized. All doped metal oxides were prepared by aerosol spray pyrolysis [20,21] whereby precursors of metal salts aqueous solutions are continuously atomized into droplets and thermally decomposed to metal oxide particles (for details see the supplementary information). Briefly, 0.2 M precursor solution, containing stoichiometric nitrates was atomized by a nebulizer to generate nominally 1 μm droplets with compressed air. The atomized droplets flowed through a diffusion dryer, where most of the water was absorbed, leaving solid precursor particles which were then passed to a tubular furnace, set at 1050 °C for doped perovskites and 750 °C for doped Bi_2O_3 to produce the desired doped metal oxide particles.

Table 1 Aerosol spray synthesized doped perovskites and Bi_2O_3 with abbreviation

Doped Perovskite	*Doped Bi_2O_3*	Abbr.
$LaCrO_3$	$(Y_{0.15}Bi_{0.85})_2O_3$	YSB15
$La_{0.8}Sr_{0.2}CrO_{3-\delta}$	$(Y_{0.3}Bi_{0.7})_2O_3$	YSB30
$La_{0.6}Sr_{0.4}CrO_{3-\delta}$	$(Y_{0.4}Bi_{0.6})_2O_3$	YSB40
$LaFeO_3$	$(W_{0.05}Bi_{0.95})_2O_{3.15}$	WSB5
$La_{0.8}Sr_{0.2}FeO_{3-\delta}$	$(W_{0.1}Bi_{0.9})_2O_{3.3}$	WSB10
$La_{0.6}Sr_{0.4}FeO_{3-\delta}$	$(W_{0.15}Bi_{0.85})_2O_{3.45}$	WSB15
$LaCoO_3$	$(W_{0.2}Bi_{0.8})_2O_{3.6}$	WSB20
$La_{0.8}Sr_{0.2}CoO_{3-\delta}$	$(Er_{0.15}Bi_{0.85})_2O_3$	ESB15
$La_{0.6}Sr_{0.4}CoO_{3-\delta}$	$(Dy_{0.15}Bi_{0.85})_2O_3$	DSB15
	$(Dy_{0.1}W_{0.05}Bi_{0.85})_2O_{3.15}$	DWSB10
	$(Dy_{0.05}W_{0.1}Bi_{0.85})_2O_{3.3}$	DWSB5
	$(Dy_{0.05}Nb_{0.1}Bi_{0.85})_2O_{3.2}$	DNSB

Fuel/Doped Metal Oxide Compositions.

Nano aluminum particles (~50 nm, 81 wt% active) were purchased from Novacentrix Corporation, nano-sized carbon black (~50 nm, ~100% active) was obtained from Cabot Corporation, nano boron particles (SB99, ~60 nm, 70 wt% active) were obtained from the SB Boron Corporation and nano tantalum powders (<50 nm, 70 wt% active) were purchased from Global Advanced Metals. Stoichiometric mixtures of fuel (Al, B, Ta, C) and doped metal oxides were mixed respectively and then sonicated in hexane for 30 min. For control of stoichiometry, the Al_2O_3 shell (19% of the mass), B_2O_3 shell (30% of the mass) and Ta_2O_5 shell (30% of the mass) content were accounted for.

Characterization.

The crystal structures and morphology of the as-synthesized metal oxides were characterized by X-ray diffraction (XRD) performed on a Bruker D8 diffractometer with Cu Kα radiation and scanning electron microscopy (SEM) conducted on a

Hitachi SU-70 instrument respectively. Le Bail refinement of all diffraction patterns was performed with the TOPAS 4.2 software.[22] Size distributions were obtained by measuring 300 individual nanoparticles statistically from SEM images of each sample, using Nano Measurer 1.2 image analysis software.

Temperature-Jump Measurement.

Initiation temperature of fuel/metal oxide and oxygen release temperature (in the absence of fuel) from individual oxidizer were measured with T-Jump/TOFMS [23,24] coupled with high-speed camera (Vision Research Phantom v12.0) operating at 67056 frames/s, using direct optical emission. A hexane suspension of samples was droppered onto a 70 um diameter platinum filament, which was heated at a rapid rate ~ 4×10^5 °C/s, to ~1200 °C within 3 milliseconds. The filament was directly inserted into the vacuum ionization region of a TOFMS, where the gaseous products could be temporally analyzed. The temperature of the wire was determined from electric resistance based on the Callendar-Van Dusen equation, through a simultaneously measure of temporal applied voltage and current. The ionization/extraction region of the TOFMS was pulsed at 10 kHz resulting in a full mass spectrum every 100 μs. A 600 MHz digital oscilloscope was used for data acquisition with a sampling rate of 100 mega sample per second.

Due to the size of nanoparticles compared with the wire and based on our previous result, the temperature of the wire is essentially equal to the temperature of the oxidizer system.[25]

Results and discussion

Structure and morphology

As example XRD patterns for the as-synthesized doped Bi_2O_3 are shown in Fig. 1. Based on Le Bail refinements, all the synthesized doped Bi_2O_3 were in the δ-phase with a single cubic Fm-3m space group, and the lattice parameters are listed in Table S1. The XRD patterns for all synthesized perovskites and refined results are shown in Fig. S1 and S2 with all perovskites in pseudocubic structures. Thus it is reasonable to argue that within each system type, the doped metal oxides have essentially the same crystal structure, and we can eliminate crystal structure as a controlling impact on initiation temperature of redox reaction with fuel.

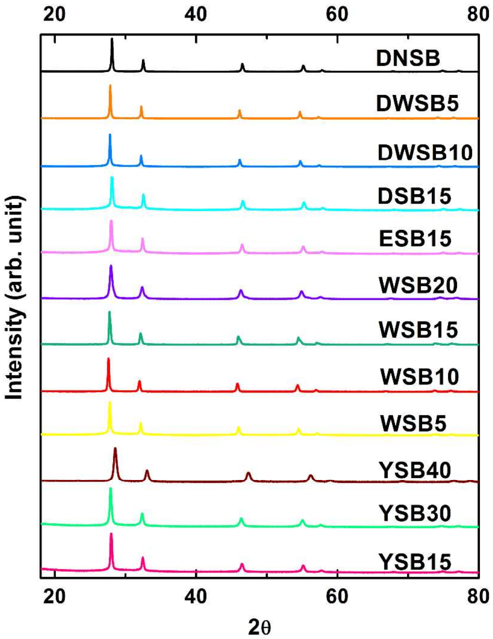

Fig. 1 *X-ray diffraction patterns of aerosol spray synthesized doped* Bi_2O_3.

Fig. 2 shows SEM images of (a) $LaFeO_3$, (b) $La_{0.8}Sr_{0.2}FeO_3$ and (c) $LaCrO_3$ as representative powders and the particle size distributions are shown in Fig. S3, indicating essentially the same morphology and particle size distribution, consistent with our previous results.[7-9,26] Similar results were found for doped Bi_2O_3 shown in

Fig. S4. Thus in this study we are able to ensure that all oxides have the same morphology and particle size distribution, eliminating these factors as variables impacting initiation temperature.

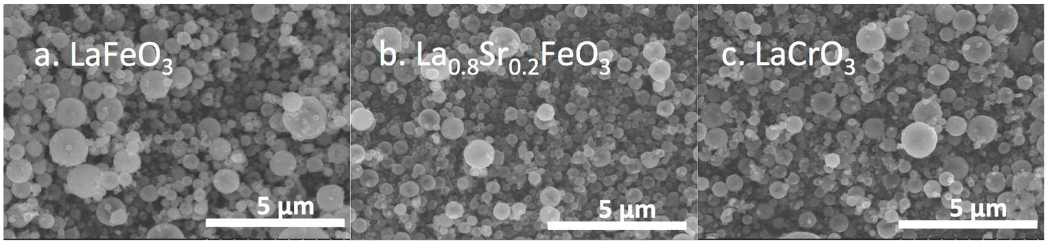

Fig. 2 *SEM image of as synthesized (a)* $LaFeO_3$*, (b)* $La_{0.8}Sr_{0.2}FeO_3$ *and (c)* $LaCrO_3$ *as representative powders*

Reaction mechanism

Two important measurables relevant to understanding reactivity, are the reaction threshold itself, and if and when oxygen gas is released from the oxidizer. Oxygen release temperatures of synthesized doped metal oxides were measured with T-jump/TOFMS. Metallic fuel (Ta, Al) or metalloid fuel (B) reacted with metal oxides vigorously with an easily discernable visible initiation event. Initiation was determined as the onset of optical emission. In contrast to Al, Ta and B, the C/metal oxide reaction is much less vigorous with no visible emission, and thus we employed the temporal CO_2 release to define the reaction threshold (For more details see the supplementary information).

The observed oxygen release temperature from the neat metal oxides and the observed initiation temperature of Al, B, C, Ta/perovskites are shown in Fig. 3. What this result shows is that almost all data points lie above the diagonal, indicating that reaction initiation occurs before oxygen (O_2) is released into the gas phase by the perovskite. Further for the temperature regime that T-jump/TOFMS could reach (~1350 °C), no O_2 release of $LaCrO_3$ and $LaFeO_3$ and no initiation of fuel/$LaCrO_3$

were observed. The results from Fig. 3 demonstrate that since initiation occurs at a temperature below which oxygen is evolved from the oxidizer, we must conclude the reaction takes place by condensed state redox reaction rather than gas evolution of oxygen leading to subsequent reaction. For doped Bi_2O_3, we have previously justified that initiations are in the condensed phase.[8]

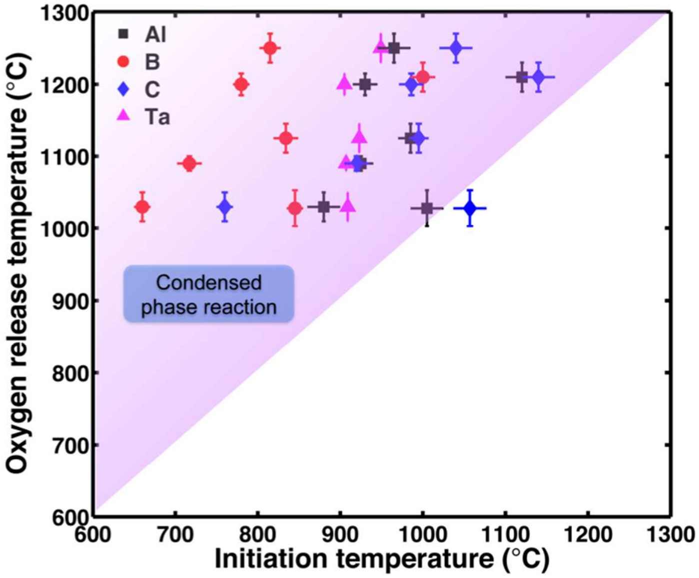

Fig. 3 *Oxygen release temperature from the perovskites vs. initiation temperature for Al/perovskite, B/perovskite, C/perovskite and Ta/perovskite, indicates that redox initiation occurs prior to oxygen release (i.e. condensed state reaction).*

Bond energy and $[V_O^{\cdot\cdot}]$ vs. initiation temperature

In our previous work, we have justified that for Al/Bi_2O_3 and Al/perovskite composites, oxygen ion transport limits the condensed phase initiation.[7,8] We also find that smaller metal-oxygen bond energy and larger oxygen vacancy concentration in doped perovskite or Bi_2O_3, lower the initiation temperature. In this study, for the purposes of tweezing out mechanistic information we expand the fuels to include B, Ta and C. Thus we have four different fuels (Al, B, Ta, C) with completely different physical properties.

The metal-oxygen bond energy for doped metal oxide can be estimated based on its stoichiometry, coordination numbers and thermodynamic data. Since for *Pm-3m* cubic, *Pnma* orthorhombic or *R3c* rhombic perovskite, A-site cations are 12-coordinated with oxygen, and B-site cations are 6-coordinated with oxygen, the average bond energy (ABE) of the perovskite can be estimated based on equation 1, where $\Delta H_{A_mO_n}$ and $\Delta H_{B_mO_n}$ are the heats of formation of A_mO_n and B_mO_n oxides at 298 K, respectively, ΔH_A and ΔH_B are the heats of sublimation of A-metal and B-metal at 298 K and D_{O_2} is the dissociation energy of gaseous oxygen.[27,28] For fluorite type doped δ-Bi_2O_3 in which that cation is 6-coordinated with oxygen anions, the average metal-oxygen bond energy is estimated based on equation 2 and 3, where a is the dopant molar ratio. Since δ-Bi_2O_3 has a defect fluorite-type crystal structure (AX_2) in which 25% of the oxygen sites in the unit cell are vacant,[29] oxygen vacancy concentration, $[V_O^{\cdot\cdot}]$ of doped δ-Bi_2O_3 can thus be estimated based on the percentage of vacant oxygen sites in one unit cell, and the lattice parameter as reported in our previous literature.[8] The calculated ABE of both doped perovskites and δ-Bi_2O_3 and $[V_O^{\cdot\cdot}]$ of doped δ-Bi_2O_3 are listed in Table S5.

$$ABE_{perovskite} = \frac{1}{2}\left(\frac{1}{12m}\left(\Delta H_{A_mO_n} - m\Delta H_A - \frac{n}{2}D_{O_2}\right) + \frac{1}{6m}\left(\Delta H_{B_mO_n} - m\Delta H_B - \frac{n}{2}D_{O_2}\right)\right) \quad (1)$$

$$ABE_{doped\ Bi_2O_3} = (1-a)\cdot\Delta(A-O) + a\cdot\Delta(A'-O) \quad (2)$$

$$\Delta(A-O) = \frac{1}{6m}\left(\Delta H_{A_mO_n} - m\Delta H_A - \frac{n}{2}D_{O_2}\right) \quad (3)$$

The calculated ABE of doped perovskite and Bi_2O_3, and the corresponding measured initiation temperature with different fuels is shown in Fig. 4. It is apparent that in each system, although four fuels were used, the initiation temperature generally increases with average M-O bond energy in the oxidizer, indicating that the redox initiation was mainly dominated by oxygen transport of metal oxide. We were surprised by these results. Four fuels with very different physical properties show similar trends with two very different oxidizer families. Within each oxidizer family all fuels appear to behave similarly, but each oxidizer family shows distinctive behavior. This result implies that the initiation of a fuel/metal oxide redox reaction relies mainly on the microscopic property of metal oxide. *We may conclude, there is a general trend that suggests an oxidizer control mechanism, regardless of fuel type.*

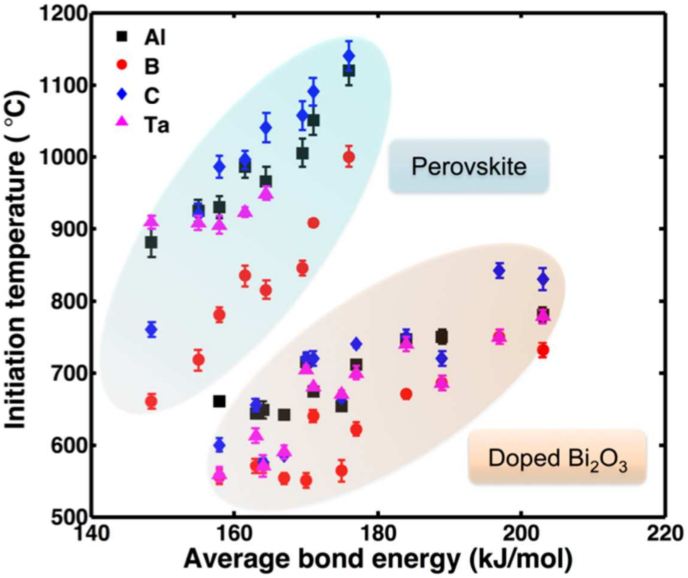

Fig. 4 *Observed relationship between average bond energy (ABE) of all doped metal oxides against the initiation temperatures of four fuels Al-B-C-Ta.*

Obviously of course, if the fuel has no role, then the data points for all fuels would be overlaid. But clearly the differences between fuels are larger than the experimental uncertainties. Within each oxidizer group, boron clearly has the lowest initiation temperature, and tantalum and aluminum have similar initiation temperatures for initiation temperatures above the aluminum melting point (660 °C). Thus there are physical aspects to the fuel that also impact the initiation temperature. This is most clearly seen in aluminum where the reaction threshold for all doped metal oxides was above ~660 °C (melting point of Al). All doped metal oxides reacted with boron above ~520 °C (above the melting point of B_2O_3 shell, 450 °C), so molten B_2O_3 wets the oxidizer creating an interface for oxygen transport as previously reported by us.[30] Carbon has the highest initiation temperature, which might be considered odd given the lack of an oxide shell. However, thermodynamically it has the least negative Gibbs free energy and is entropy driven process as compared to the other fuels that are enthalpy driven. As an example, the heat of reaction (ΔH_r) and Gibbs free energies (ΔG_r) of Al, B, C, Ta reacted with pure Bi_2O_3 is computed at the initiation point and shown in Table 2.[8,30] C/Bi_2O_3 shows the least negative ΔG_r compared to Al/Bi_2O_3, B/Bi_2O_3 and Ta/Bi_2O_3, but perhaps more importantly, because it is almost thermo-neutral (least negative ΔH_r), there is no significant generated heat that can overwhelm the heat losses, and is probably why the reaction of carbon/metal oxide is so poor and initiation occurs at a higher temperature.

Table 2. Calculated heat of reaction and Gibbs free energy for Al, B, C, Ta with pure Bi_2O_3 at the initiation point.

Composite	Initiation temperature (°C)	ΔH_r (kJ/mol)	ΔG_r (kJ/mol)
$Al+1/2Bi_2O_3 – 1/2Al_2O_3+Bi$	630±25	-554	-558
$B+1/2Bi_2O_3 – 1/2B_2O_3+Bi$	540±25	-348	-363
$C+2/3Bi_2O_3 – CO_2+4/3Bi$	630±25	-20	-236
$Ta+5/6Bi_2O_3 – 1/2Ta_2O_5+5/3Bi$	630±25	-547	-600

Tantalum as fuel appears to be not sensitive to the ABE of oxidizer, especially with perovskite oxides, indicating the initiation of Ta/metal oxide is more fuel sensitive, especially with less oxygen active oxidizer. It is reported that metal oxides react with Ta, when cracks appeared in the Ta_2O_5 shell due to its amorphous to crystalline phase change. These cracks serve as channels for oxygen ion diffuse to the tantalum core.[31]

Not surprising then that Ta is less sensitive to the oxidizer, although the general bond energy trends still tend to hold.

The fact that the two systematic oxidizers do not overlay implies other parameters come into play besides that average bond energy. Presumably this would include oxygen vacancy concentration, $[V_O^{\cdot\cdot}]$, which impacts the oxygen ion transport of metal oxides and thus metal oxide's oxidation capability.[8] The $[V_O^{\cdot\cdot}]$ of all aliovalent dopant doped δ-Bi_2O_3 vs. the initiation temperature of these doped δ-Bi_2O_3 with different fuels is shown in Fig. 5. Apparently initiation temperature decreases with $[V_O^{\cdot\cdot}]$. Thus both metal-oxygen bond energy and $[V_O^{\cdot\cdot}]$ affect the initiation temperature. The $[V_O^{\cdot\cdot}]$ of perovskites is reported to be significantly lower than that of doped δ-Bi_2O_3.[32] This difference in $[V_O^{\cdot\cdot}]$ probably leads to the discontinuity of initiation temperature vs. bond energy trend switching from doped perovskites to δ-Bi_2O_3.

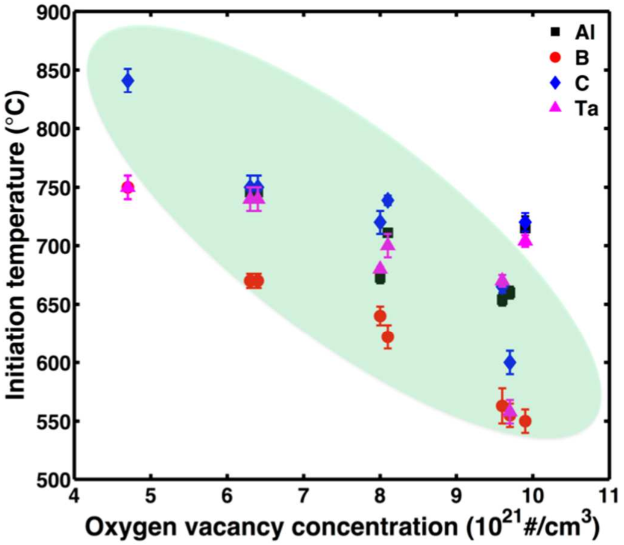

Fig. 5 *Observed relationship between oxygen vacancy concentrations of aliovalent doped δ-Bi_2O_3 vs. the initiation temperatures of four fuels Al-B-C-Ta.*

Crystal structure comparison

The differences in crystal structure between the different oxide classes could possibly be another reason impacting initiation temperature in addition to bond energy and $[V_O^{\cdot\cdot}]$. It is known that "free volume" and "critical radius" are important crystallographic parameters in oxygen ion transport.[33,34] The critical radius refers to the limit radius that mobile oxygen can pass, and the free volume is obtained by subtracting the volume of all constituent ions from the overall unit cell volume. It would be reasonable to expect that a larger critical radii and free volume results in faster oxygen ion transport and thus a lower initiation temperature. With doped perovskites in Pm-3m, Pnma, or R-3c space groups and doped Bi_2O_3 in Fm-3m space group, the oxygen ion experiences different degrees of openness in the lattice. Consider the cubic $La_{0.6}Sr_{0.4}CoO_3$ (space group: Pm-3m) and $(Y_{0.15}Bi_{0.85})_2O_3$ (space group: Fm-3m) as representative for perovskite and the doped Bi_2O_3 respectively. As both systems under consideration are high symmetry cubic structures, we can compare the ion arrangements on (111) lattice planes in Fig. 6. It is quite clear that oxygen ions are more tightly packed in $La_{0.6}Sr_{0.4}CoO_3$ than in $(Y_{0.15}Bi_{0.85})_2O_3$, which should manifest itself with a higher ion-mobility for the bismuth oxide. This can be seen more quantitatively by calculating the critical radius and free volume per oxygen ion in Table 3. One sees that doped Bi_2O_3 has much larger free volume and a larger critical radius than doped perovskite, consistent with its elevated oxygen ion mobility. This may be partially responsible for the lower redox initiation temperature for the same ABE for the doped Bi_2O_3 relative to the perovskites.

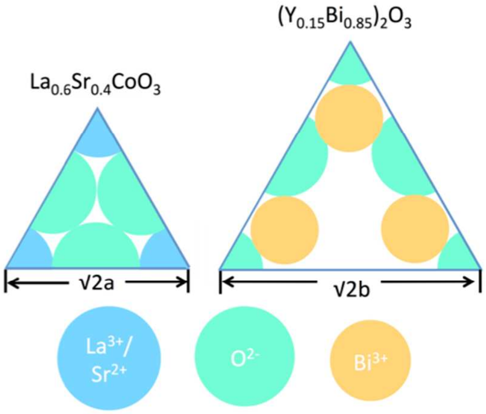

Fig. 6 *Schematic view of the (111) lattice plane of a cubic unit cell* $La_{0.6}Sr_{0.4}CoO_3$ *and* $(Y_{0.15}Bi_{0.85})_2O_3$ *(same length scale), a and b are the lattice parameters for* $La_{0.6}Sr_{0.4}CoO_3$ *and* $(Y_{0.15}Bi_{0.85})_2O_3$ *respectively.*

Table 3 The critical radius and free volume per oxygen ion in $(Y_{0.15}Bi_{0.85})_2O_3$ and $La_{0.6}Sr_{0.4}CoO_3$

	Critical radius (Å)	Free volume/oxygen ion ($Å^3$)
$La_{0.6}Sr_{0.4}CoO_3$	0.87	3.2
$(Y_{0.15}Bi_{0.85})_2O_3$	1.02	14.4

Electronegativity vs. initiation temperature

One of the major results of this work thus far is that the strength of the metal–oxygen bond is critical to understanding initiation. Since the strength of a M–O bond can be related to the ionic nature of the interaction we have previously explored electronegativity as a potentially even simpler metric.[7,16] A larger electronegativity difference between metal and oxygen should yield a more ionic bond, and thus a more stable structure, because the degree of hybridization between metal and oxygen depends on the electronegativity difference, and electronegativity is the average of the ionization potential and the electron affinity. Fig. 7 shows clearly that initiation temperature increases with increasing electronegativity difference χ, in the metal oxide, calculated on the Pauling Scale,[35] and that higher ionic character increases initiation temperature. Thus electronegativity appears to be a very effective simple metric determining the initiation temperature. Individual plots between electronegativity difference and initiation temperature for oxidizer with different fuels are shown in Fig. S7. The electronegativity difference covers a larger range for doped Bi_2O_3 (3.08-4) than for doped perovskites (3.6-4.1). Individual trends for different fuels are similar as Fig. 4 with boron having the lowest initiation temperature and carbon having the highest initiation temperature.

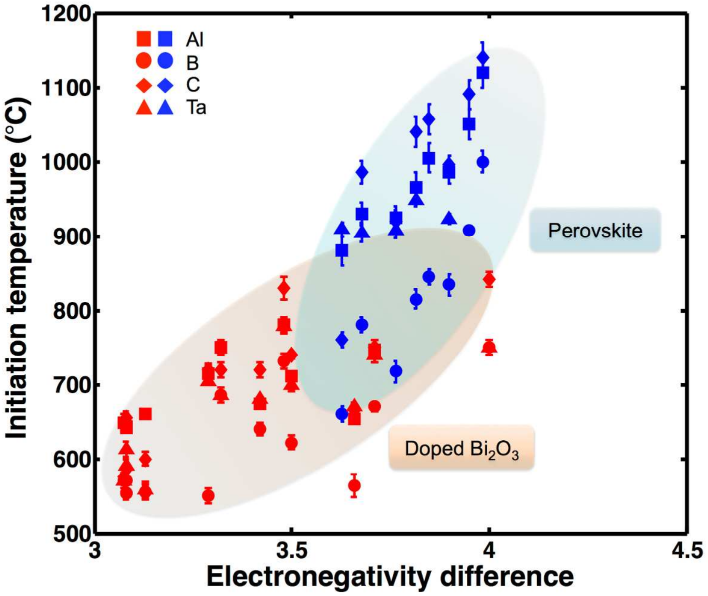

Fig. 7 *Overall electronegativity difference of doped metal oxide versus initiation temperature of Al/B/C/Ta with doped metal oxides with blue symbols for perovskite oxides and red symbols for doped* Bi_2O_3

Conclusions

The goal of this paper was to explore what atomic properties of an oxidizer can be correlated to reactivity with solid elemental fuels. This was evaluated using two systematic doped metal oxides: perovskites and δ-Bi_2O_3, sharing the same crystal structure and morphology within each system, as oxidants with four fuels (Al, B, C, Ta) with very different physical and chemical properties. We found that, within each oxidizer family, initiation temperature increases with M-O bond energy of the oxidizer, seemingly independent of fuel type. The absolute value for initiation of perovskites and δ-Bi_2O_3 doesn't overlap, which we attribute to differences in oxygen vacancy concentration and crystal structure in these two groups of metal oxides. We also found that initiation temperature increased with the electronegativity difference of oxidizer for all four fuels, indicating electronegativity might be a simpler metric than metal-oxygen bond energy to evaluate the reaction threshold.

Acknowledgements

This work was supported by the Army Research Office and the Defense Threat Reduction Agency.

References

1. E. L. Dreizin, *Prog. Energy Combust. Sci.*, 2009, **35**, 141-167.
2. W. Zhou, J. B. DeLisio, X. Wang and M. R. Zachariah, *Combust. Flame*, 2017, **177**, 1-9.
3. S. Apperson, R. V. Shende, S. Sunramanian, D. Tappmeyer, S. Gangopadhyay, Z. Chen, K. Gangopadhyay, P. Redner, S. Nicholich and D. Kapoor, *Appl. Phys. Lett.,* 2007, **91**, 3109-3111.
4. G. Jian, S. Chowdhury, K. Sullivan and M. R. Zachariah, *Combust. Flame,* 2013, **160**, 432-437.
5. E. L. Dreizin, *Combust. Flame,* 1996, **105**, 541–556.
6. D. Sundaram, V.Yang, and R. A. Yetter, *Prog. Energy Combust. Sci.,* 2017, **61**, 293-365.
7. X. Wang, T. Wu and M. R. Zachariah, *J. Phys. Chem. C,* 2017, **121**, 147-152.
8. X. Wang, W. Zhou, J. B. DeLisio, G. Egan and M. R. Zachariah, *Phys. Chem. Chem. Phys.,* 2017, **19**, 12749-12758.
9. X. Wang, R. Jayathilake, D. D. Taylor, E. E. Rodriguez and M. R. Zachariah, *J. Phys. Chem. C,* 2018, *122*, 8796-8803.
10. Y. H. Huang, R. I. Dass, Z. L. Xing and J. B. Goodenough, *Science,* 2006, **312**, 254-257.
11. W. H. Kan, A. J. Samson and V. Thangadurai, *J. Mater. Chem. A*, 2016, **4**, 17913-17932.

12. J. Zhu, H. Li, L. Zhong, P. Xiao, X. Xu, X. Yang, Z. Zhao and J. Li, *Acs Catal.*, 2014, **4**, 2917-2940.
13. Y. Xiao, W. Zhu, G. Cai, M. Chen, Y. Zheng, F. Zhong and L. Jiang, *Phys. Chem. Chem. Phys.,* 2017, **19**, 30418-30428.
14. X. Y. Wu, L. Chang, M. Uddi, P. Kirchen and A. Ghoniem, *Phys. Chem. Chem. Phys.,* 2015, **17**, 10093-10107.
15. Z. Sarshar, F. Kleitz and S. Kaliaguine, *Energy Environ Sci.*, 2011, **4**, 4258-4269.
16. L. Liu, D. D. Taylor, E. E. Rodriguez and M. R. Zachariah, *Chem. Commun.,* 2016, **52**, 10369-10372.
17. S. Hull, S. T. Norber, M. G. Tucker, S. G. Eriksoon, C. E. Mohn and S. Stolen, *Dalton Trans.,* 2009, **40**, 8737-8745.
18. T. Takahashi, H. Iwahara and Y. Nagai, *J. Appl. Electrochem.,* 1972, **2**, 97-104.
19. T. Wu, X. Wang, J. B. DeLisio, S. Holdren and M. R. Zachariah, *Carbon*, 2018, **130**, 410-415.
20. T. Wu, A. SyBing, X. Wang and M. R. Zachariah, *J. Mater. Res.,* 2017, **32**, 890-896.
21. G. Jian, J. Feng, R. J. Jacob, G. C. Egan and M. R. Zachariah, *Angew. Chem. Int. Ed.*, 2013, **52**, 9743-9746
22. R. W. Cheary and A. A. Coelho, *J. Appl. Crystallogr.*, 1992, **25**, 109-121.
23. L. Zhou, N. Piekiel, S. Chowdhury and M. R. Zachariah, *Rapid Commun. Mass Spectrom.,* 2009, **23**, 194–202.
24. G. Jian, N. W. Piekiel and M. R. Zachariah, *J. Phys. Chem. C,* 2012, **116**, 26881-26887.
25. S. Chowdhury, K. Sullivan, N. Piekiel, L. Zhou and M. R. Zachariah, *J. Phys. Chem. C,* 2010, **114**, 9191-9195.
26. L. Liu, M. R. Zachariah, S. I. Stoliarov and J. Li, *RSC Advances.,* 2015, **5**, 101745-101750.
27. S. Li, W. Jin, P. Huang, N. Xu and J. Shi, *Ind. Eng. Chem. Res.,* 1999, **38**, 2963-2972.
28. D. R. Lide, Standard Thermodynamic Properties of Chemical Substances. *CRC handbook of Chemistry and Physics*. 2007, **5**.
29. H. A. Harwig, *Zeitschrift für anorganische und allgemeine Chemie,* 1978, **444**, 151-166.
30. X. Wang, T. Wu, H. Wang, J. B. DeLisio, Y. Yang and M. R. Zachariah, *Combust. Flame*, 2018, **197**, 127-133.
31. J. B. DeLisio, X. Wang, T. Wu, G. Egan, R. Jacob and M. R. Zachariah, *J. Appl. Phys.,* 2017, **122**, 245901.
32. M. Dawber and J. F. Scott, *Appl. Phys. Lett.,* 2000, **76**, 1060-1062.
33. M. Mogensen, D. Lybye, N. Bonanos, P. V. Hendriksen and F. W. Poulsn, *Solid State Ionics,* 2004, **174**, 279-286.
34. D. Lybye, F. W. Poulsen and M. Mogensen, *Solid State Ionics,* 2000, **128**, 91-103.
35. L. Pauling, *J. Am. Chem. Soc.*, 1932, **54**, 3570-3582.